Applied Catalysis B: Environmental 259 (2019) 118019

Contents lists available at ScienceDirect

Applied Catalysis B: Environmental

journal homepage: www.elsevier.com/locate/apcatb

The importance of inner cavity space within Ni@SiO_2 nanocapsule catalysts for excellent coking resistance in the high-space-velocity dry reforming of methane

Changzhen Wang[a], Xiangyu Jie[b], Yuan Qiu[a], Yongxiang Zhao[a,*], Hamid A. Al-Megren[c], Saeed Alshihri[c], Peter P. Edwards[b,*], Tiancun Xiao[a,b,**]

[a] Engineering Research Center of Ministry of Education for Fine Chemicals, Shanxi University, Taiyuan 030006, PR China
[b] Inorganic Chemistry Laboratory and King Abdulaziz City for Science and Technology-Oxford Centre of Excellence in Petrochemicals (KOPRC), University of Oxford, Oxford, OX1 3QR, UK
[c] Materials Science Research Institute, King Abdulaziz City for Science and Technology (KACST), P. O. Box6086, Riyadh, 11442, Saudi Arabia

ARTICLE INFO

Keywords:
Ni@SiO_2 nanocapsule catalysts
Inner cavity space
High-space-velocity
Dry reforming
Coking resistance

ABSTRACT

Metal sintering and carbon deposition are acknowledged to be the foremost critical issues in the important energy storage process of high temperature Dry Reforming of Methane (DRM). For that process, so-called "core-shell catalysts" have exhibited outstanding catalytic performance. However, the intrinsic confined geometric space of the host core-shell structure not only inevitably limits the ability of the catalyst system to facilitate the critical rapid infusion and diffusion of reacting gases, but also enhances the accompanying conversion of carbon intermediates to inert, catalyst-deactivating carbonaceous deposits under high-space-velocity conditions. Herein, we present a study highlighting the importance of the inner cavity space, now of a quasi-zero-dimensional, tubular, yolk-shell structured Ni@SiO_2 nanocapsule catalyst, in the DRM process. The tubular yolk-shell structured Ni@SiO_2 nanocapsule catalysts having controlled inner cavities (5.0–13.0 nm × 5.0–50.0 nm dimensions) were synthesised via a water-in-oil micro-emulsion method by employing different aging times (i.e. 3 h, 6 h and 12 h). Compared with corresponding Ni@SiO_2 nanosphere catalysts, the tubular nanocapsule catalysts displayed both excellent catalyst activity, stability, and (metal) anti-sintering ability with, equally important, negligible carbon deposition during the operating DRM process under high space velocity conditions (60 L g^{-1} h^{-1}), most relevant for application in real industrial processes.

1. Introduction

Energy-related carbon dioxide emissions grew by 1.7% in 2018 to a historic high of 33bn tonnes, according to the International Energy Agency [1]. In addition, the total content of another greenhouse gas, methane, in the atmosphere is estimated to increase by some 0.9% per year in the near future [2]. There is therefore increasing interests in what we here term "Co-Utilisation" of both these greenhouse gases – CO_2 and CH_4 - to produce chemicals and fuel, whilst at the same time targeting a reduction in total greenhouse emissions [3]. Such approaches have included: CO_2 hydrogenation [4,5], CO_2 electrochemical reduction [6], partial oxidation of methane [7], steam reforming of methane [8,9] and Dry Reforming of Methane (DRM) [10,11] etc. Amongst these options, a common target over the past few decades has been the production of so-called Synthesis Gas - "Syn Gas" (a combination of CO and H_2), particularly with a molar ratio of 1:1 produced by DRM which can then be used directly as a versatile feedstock for Fischer–Tropsch synthesis to yield products such as gasoline-range fuels and dimethyl ether [11–13].

Ni-based catalysts are currently widely used in DRM reactions due to their comparable catalytic activity to noble metals and their relatively inexpensive cost [14]. However, the sintering of Ni active metal catalyst particles and severe carbon deposition under the high temperature reactions operating in the DRM process are major challenges limiting their large scale industrial applications. One of the most important factors in improving the performance of Ni-based catalysts for DRM lies in the careful control of the catalyst particle size, together with their effective confinement (localisation) in specific sites on

* Corresponding authors.
** Corresponding author at: Engineering Research Center of Ministry of Education for Fine Chemicals, Shanxi University, Taiyuan 030006, PR China.
E-mail addresses: yxzhao@sxu.edu.cn (Y. Zhao), peter.edwards@chem.ox.ac.uk (P.P. Edwards), xiao.tiancun@chem.ox.ac.uk (T. Xiao).

https://doi.org/10.1016/j.apcatb.2019.118019
Received 16 May 2019; Received in revised form 22 July 2019; Accepted 27 July 2019
Available online 30 July 2019
0926-3373/

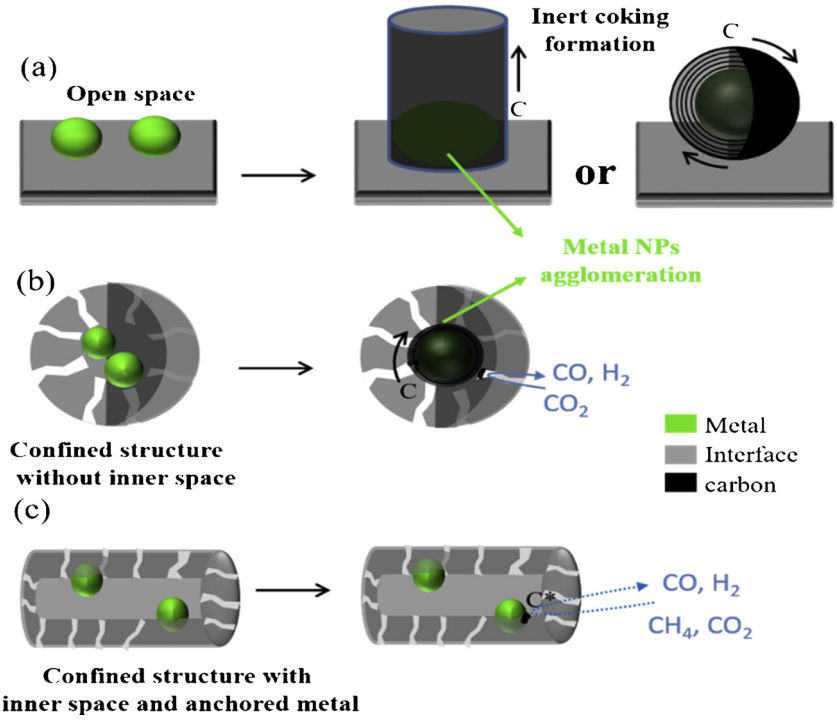

Scheme 1. A schematic representation of various metal-interface structures and their possible roles during the dry reforming of methane reaction. (a) Normal supported metal particles, (b) encased metal particles in a core-shell structure, and (c) anchored metal particles in a hollow capsule, exemplified in this work.

support materials to inhibit the troublesome catalyst sintering and aggregation process. Thus, many researchers have investigated metal particle size control and confinement methods through the enhancement of metal-support interactions [15,16]. For instance, Zhang et al. reported a series of LDH-derived and boron nitride modified Ni catalysts, in which the confinement strategy can embed well-dispersed Ni nanoparticles and prevent their sintering during the DRM process [17–19]. However, the control of metal particle size during any high temperature catalytic process is always challenging due to the inevitable sintering or coagulation of metal particles via Ostwald ripening [20,21]. Furthermore, most of these cited investigations produced the active Ni catalysts via impregnation or co-precipitation methods. A critical drawback of both these synthetic methods is that external space *above* the metal sites is necessarily always accessible to participating reagent, therefore making it difficult to inhibit both metal sintering and carbon deposition, leading to inevitable catalyst deactivation [22,23] (Scheme 1a).

Recently, core-shell structured Ni-based catalysts deliberately embedded in highly porous silica hosts have been investigated to inhibit active metal catalyst sintering in high temperature reactions [7,24,25]. Such approaches have great potential in industrial applications due to the relatively simple preparation method and high efficiency [26]. Notably, a “dressed” porous silica shell around such metal particles plays a vital role in inhibiting the movement and subsequent growth of the active metal catalyst by effectively encapsulating the catalyst, whilst also producing outstanding catalytic stability [27]. Moreover, the embedded core-shell structure can also inhibit the formation and growth of carbon species on metal surfaces, a process known to be highly detrimental to the catalytic process by reducing the number of active catalytic sites and causing a concomitant catalyst deactivation [28]. However, more recent work has revealed the negative result that tailored spherical Ni@SiO_2 nanoparticles did not produce a high catalytic stability for the DRM reaction under the real and invariably challenging industrial operating conditions of very high space velocity [29]. It was found that under these conditions, many inner metal sites of core-shell structure were covered by the close contacted dense SiO_2 shell, leading to the inability of the metal catalysts to keep up with both the rapid pace of diffusion and conversion of reactants [30] (Scheme 1b). Zhang et al. [31] and Bian et al. [32] proposed the use of a type of “Two-open-ends” tubular multicore-shell catalyst derived from nickel-phyllosilicate nanotubes for both hydrogen production via steam reforming and dry reforming reactions. They pointed out that the unique one-dimensional Ni/SiO_2 nanotube structure (in terms of incoming reactants and outgoing products) can effectively limit the growth or aggregation of catalyst nanoparticles under thermal condition below 700 °C. However, their results showed that once the reaction temperature moves above 700 °C, this end-opened, one-dimensional Ni/SiO_2 nanotube structure will begin to be destroyed, and the encapsulated Ni nanoparticles consequently increase in size. Therefore, the one-dimensional structure appears unsuitable when applied to the higher reaction temperature range characteristic of any industrial DRM process.

Compared to the core-shell sphere structure materials and the two-open-ends tubular multicore-shell catalysts discussed above, a yolk-shell catalyst with inner cavity space has clear additional advantages [29,33]. For instance, Zhao et al. [34] proposed that a yolk-shell framework could provide a greater availability of active metal catalyst centres for the incoming reactant molecules. Dahlberg et al. [35] theorised that such a configuration could also facilitate the accumulation of reactants, intermediates, and products in the local environment of metal particles. However, any significant increase of the inner cavity space will necessarily break the confinement framework over the inner metal particles and lead to carbon formation [31,32]. While the effect of the cavity size of yolk-shell catalysts for operational high space velocity dry reforming of methane has seldom been reported; such conditions are obviously critical for any industrial-scale applications of the dry reforming process.

Here, in order to investigate the influence of the cavity size of enclosed tubular yolk-shell catalysts under high space velocity DRM conditions, we prepared a series of highly dispersed Ni@SiO_2 nanocapsule catalysts with various inner cavities together with a dense Ni@SiO_2 nanosphere catalyst and investigated their comparative catalytic performance under high space velocity conditions. The Ni@SiO_2

nanocapsule catalysts with a particular cavity dimension showed greatly improved catalytic activity and stability compared with Ni@SiO_2 nanosphere catalyst under comparable high space velocity conditions. It appears that the two-dimensional-confined inner cavity contributes to an enhanced adsorption and mass transfer with respect to incoming reactant molecules and can provide significantly more active sites [33,34] (Scheme 1c). Furthermore, both the confinement effect of nanocapsule structure and the anchoring effect on Ni sites are also responsible for the stabilization of the Ni nanoparticles in the DRM reaction.

2. Experimental

2.1. Chemicals

$Ni(NO_3)_2{\cdot}6H_2O$, $N_2H_4{\cdot}H_2O$ and C_6H_{12} were bought from Sinopharm Chemical Reagent. Brij C10 ($C_{16}H_{33}(OCH_2CH_2)_nOH$, n ~ 10) was obtained from Sigma-Aldrich. Tetraethylorthosilicate (TEOS) was bought from Aladdin.

2.2. Preparation of Ni@SiO_2 nanocapsule

Yolk-shell Ni@SiO_2 nanocapsules (Ni@SNC) with various inner cavities were prepared by a reverse micelle approach as described elsewhere [30]. In a typical water-in-oil system, $Ni(NO_3)_2$ aqueous solution is used as the Ni precursor and C_6H_{12} is the oil phase of the microemulsion. Brij C10 is used as a non-ionic surfactant, while $N_2H_4.H_2O$ is used as the complexing and reducing agent of the nickel precursor. The microemulsion system was obtained by mixing 5 mL 1.8 M $Ni(NO_3)_2$ aqueous solution into 100 mL 0.5 M Brij C10 oil solution. Next, $N_2H_4.H_2O$ was added dropwise into the microemulsion to form a purple $Ni(N_2H_4)_3^{2+}$ complex. After adding ammonia water, the obtained slurry was kept stirring with different aging time (*i.e.* 3 h, 6 h and 12 h) to prompt the decomposition of $Ni(N_2H_4)_3^{2+}$ and the elongation of capsule cavity. Following this, 10 mL of TEOS was slowly added with dramatic stirring and this was kept stirring for 12 h for the hydrolysis and condensation of TEOS. Finally, the slurry was centrifuged and washed 3 times with isopropyl alcohol. The lavender solid was dried overnight at 80 °C and then calcined at 700 °C for 5 h at a ramping rate of 2 °C/min. The as-prepared Ni@SiO_2 nanocapsule catalysts were nominated as Ni@SNC-A3, Ni@SNC-A6 and Ni@SNC-A12 according to their different aging time.

2.3. Preparation of Ni@SiO_2 nanosphere

To investigate the importance of inner cavity space of Ni@SiO_2 catalysts under high space velocity dry reforming of methane, a core-shell Ni@SiO_2 nanosphere (Ni@SNS) catalyst was also prepared by a similar reverse micelle approach with some technical alterations. To be precise, all the material preparation steps are identical to that of Ni@SiO_2 nanocapsule except the adding sequence of $N_2H_4.H_2O$ and ammonia. Specifically, the ammonia was previously added to the microemulsion system, and kept stirring for an aging time of 3 h. Then, $N_2H_4.H_2O$ was added dropwise to the green gel and the following steps are the same as above, the prepared Ni@SiO_2 nanosphere catalyst was nominated as Ni@SNS.

The detailed catalyst characterization, catalytic test and kinetic study can be seen in ESI.

3. Results and discussion

3.1. Synthesis of Ni@SiO_2 catalysts with various inner dimension cavities

The capsule and sphere Ni@SiO_2 materials with various inner cavities were synthesised by a water-in-oil microemulsion method as illustrated schematically in Scheme 2. The different inner cavities of capsule catalysts are endogenously grown by the special micellar elongation method of this water-in-oil microemulsion system via the decomposition of $Ni(N_2H_4)_x$ in the aqueous phase ($3N_2H_4 = 4NH_3\uparrow + N_2\uparrow$ or $N_2H_4 = N_2\uparrow + 2H_2\uparrow$) [28,30,36]. The decomposition of Ni$(N_2H_4)_x$ compound has been confirmed by X-ray diffraction (XRD) analysis on pre-calcined samples (Figure S1). In this protocol, the surfactant helps to form a spherical water-in-oil micelle system but with a strong gaseous capture capacity, and metal ions can uniformly disperse inside the micelles [37,38]. After the addition of hydrazine, the insoluble $Ni(N_2H_4)_3^{2+}$ complex is formed within the micelles, and a portion of this complex can be decomposed with the extension of aging time in the presence of OH^- (NH_4OH) to produce gaseous bubbles, which leads to the perpendicular elongation of capsule micelle in a special (tubular) dimension by the gaseous products via buoyancy. After the TEOS was hydrolyzed and coated on the outer surface of the capsule micelle, a hard capping framework was formed with limited growth on the facets and the complex formation was confined [36]. It is interesting to note that the cavity formation relies on the complexation and reduction between N_2H_4 and Ni^{2+} to produce gases, and the OH- as well as the reduced Ni metal can act as a catalyst to promote the decomposition of $Ni(N_2H_4)_3^{2+}$ complex [35]. As a result, by prolonging the aging time, the OH- or reduced Ni in the micelle has a higher likelihood of catalysing the decomposition of N_2H_4 [39]. Moreover, during the wet-chemistry process, more surfactant molecules can aggregate on the water-oil interface of a micelle during a prolonged aging time [40,41], thus improving the elongation and dispersion of micelles.

Based upon prolongation of the aging time, the inner cavities of highly dispersed Ni@SiO_2 nanocapsule (Ni@SNC) materials were elongated where our TEM study has confirmed the successful formation of Ni@SiO_2 samples within different dimensions of inner cavities (Fig. 1). In Fig. 1a we show a core-shell type Ni@SiO_2 nanosphere (Ni@SNS) structure with negligible inner cavity space and a thick shell layer of 14.0 nm. This situation arises because of the limited time enabled the decomposition of $Ni(N_2H_4)_3^{2+}$ complex inside the micelles before the TEOS capping when ammonia was added ahead of N_2H_4; consequently, little gas initiator could remain inside the original micelle and this led to the persistence of a spherical core-shell structure. In contrast, a tubular inner cavity structure of highly dispersed SiO_2 nanocapsule was observed in Ni@SNC (Fig. 1b–d) with distinguishable sizes of inner cavity in the range of 5.0–50.0 nm × 5.0–13.0 nm (Fig. 1e and f). Herein, the Ni@SNC samples prepared by the different aging time of 3, 6 and 12 h are marked as Ni@SNC-A3, Ni@SNC-A6 and Ni@SNC-A12, respectively. It was found that the average inner cavity length of Ni@SNC samples was increased with the prolonged aging time while the cavity diameter remained nearly the same at around 8.0 nm. The Ni@SNC-A3 sample had the smallest average inner cavity length of about 10–20 nm, whereas some 40 nm long cavities were produced in the Ni@SNC-A12 sample whose aging time was prolonged to 12 h. Moreover, the shell thickness of Ni@SNC-A3, Ni@SNC-A6 and Ni@SNC-A12 samples are very similar, averaging around 5.0 nm (Fig. 1g).

Turning to a consideration of the nickel core particles, substantial nano and sub-nano nickel particles (1.0–2.5 nm) were produced via this route using a micellar precursor in a wet microemulsion; these particles were then dispersed within the cavities which had been encapsulated by regular shells of SiO_2. Furthermore, some nickel particles were found anchored on the inner shell of cavities (as labelled in Fig. 1b–d), which appeared to have a stronger geometric interaction with the silica support. We believe that this type of Ni NPs system has a firm stability which can in turn negate the metal agglomeration and carbon deprivation [30]. It was also observed that the samples prepared by longer aging time had smaller Ni particle size; particularly, the number of small Ni particles (< 2.5 nm) in the Ni@SNC-A6 sample was significantly increased when compared with Ni@SNC-A3 sample. In comparison to the fine nickel confinement inside the shell in Ni@SNC samples, several small nickel particles were irregularly mingled with the SiO_2 outer layer over some monomers of the Ni@SNS (Fig. 1a); and

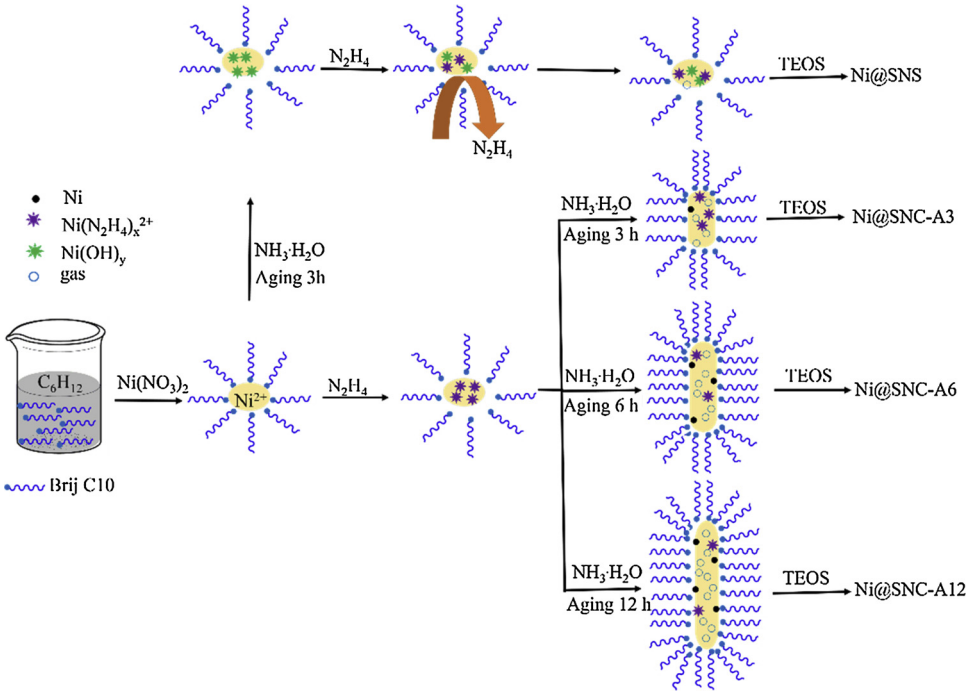

Scheme 2. Proposed cavity formation mechanism of the Ni@SiO_2 catalysts with various inner dimension cavities.

this may lead to an inferior metal confinement effect.

Other physicochemical properties of synthesised Ni@SiO_2 catalysts are listed in Table 1. Inductively Coupled Plasma-Atomic Emission Spectrometry (ICP-AES) analysis was conducted to determine the actual Ni loading in the prepared Ni@SiO_2 catalysts. As a result, Ni contents in the different aged Ni@SNC capsule catalysts were nearly the same at ca. 12.3 wt%, whereas only 10.0 wt% of Ni was detected in the Ni@SNS catalyst. The Ni dispersion was also found increased from 7.9% in the Ni@SNS catalyst to 14.4% in the Ni@SNC-A6 capsule catalysts by H_2 chemisorption. This suggests that a prolonged inner cavity dimension is favourable for producing highly dispersed Ni particles inside the SiO_2 shell by supplying more supporting interface to stabilize the sub-nano particles; and the high Ni dispersion will provide more exposed active sites for the feed gas, thereby enhancing the performance of Ni@SNC catalysts at high GHSV. However, the slightly decreased dispersion of Ni@SNC-A12 also hints that the larger-the-better inner cavity space might not be the optimum situation, i.e. when the cavity length is long enough to afford saturated interface to disperse the nano or sub-nano metal particles, the *over-spacious* interior cavity can conversely be detrimental to the process as the enclosed framework will change from capsule (quasi-zero-dimensional) to tube (one-dimensional) structure, thus sacrificing the geometric confinement for some special Ni NPs in the tubular direction.

In the study on N_2 adsorption/desorption isotherms and pore size distributions of Ni@SiO_2 catalysts (Figure S2), Ni@SNS and Ni@SNC-A3,6,12 catalysts were revealed to have mesoporous structures; and the specific surface area of Ni@SNC catalysts were found to be nearly 2.5 times higher than that of Ni@SNS catalyst. Moreover, the BJH average pore sizes of the Ni@SNC-A3,6,12 capsule catalysts were gradually increased from 9.3 nm to 12.5 nm with the increase of aging time, which is in accordance with their micelle precursor (cavity space) length (Table 1). Interestingly, the pore size distribution plots of Ni@SNC (Figure S2b) affirmed a bimodal porosity of nanocapsule structure with two types of mesoporous channels concentrated at dimensions of 3.0–4.0 nm and 8.0–20.0 nm, respectively. As reported by our previous study and that of other researchers [30,42], the former can be attributed to small pores in the silica shell, whereas the latter is derived from the inner voids of the hollow capsule. The fundamental idea of producing larger capsule cavity space, such as the situation for Ni@SNC-A6,12 catalysts is to make the catalysts more efficient in the batch conversion of an incoming gas pulse flushed into the capsule. Moreover, compared with Ni@SNS catalysts, the existence of the shell pores in Ni@SNC catalyst can potentially promote faster gas diffusion both inside and outside the host shell.

3.2. Catalytic performance of Ni@SNC catalysts for the DRM process under high-space-velocity conditions

The catalytic performance of Ni@SNC catalysts with different inner cavities for DRM was evaluated at 700 °C with an experimental GHSV of 60 L g^{-1} h^{-1}, as shown in Fig. 2. Clearly, the Ni@SNC-A3,6,12 capsule catalysts performed much better than that of Ni@SNS catalyst under comparable high-space-velocity conditions with both the methane and CO_2 conversions remaining nearly the same even after 30 h time on stream test.

In contrast, the Ni@SNS catalyst suffered a significant decrease in conversion activity. The thermodynamic equilibrium calculations (calculated via HSC chemistry) predict methane and CO_2 conversions of 72.0% and 82.0%, respectively; the slightly lower conversions observed in this study can be attributed to the reduced contact time between the incoming feedstock molecules and the catalysts under these high space velocity conditions [26]. Moreover, the H_2/CO ratio obtained is less than 1 as a result of the co-occurrence of the reverse water gas shift (RWGS) reaction; thus, the CO_2 conversion in general is about 7.0% higher than the corresponding CH_4 conversion.

Despite the observation of very little difference between the various Ni@SNC-A3,6,12 catalysts under present conditions (Table S1), the importance of different cavity space on DRM in terms of intrinsic activity and coke resistance will be illustrated shortly in both our detailed kinetic studies and post-reaction analysis.

It is noteworthy that the greatest challenge for the DRM process is to design a highly coking-resistant catalyst, operating under the characteristic industrial operation conditions of high-space-velocity. Under such conditions, the product yield efficiency can be improved, whereas, paradoxically, simultaneously accelerating the methane cracking and resulting in the accumulation of carbon intermediates, detrimental to

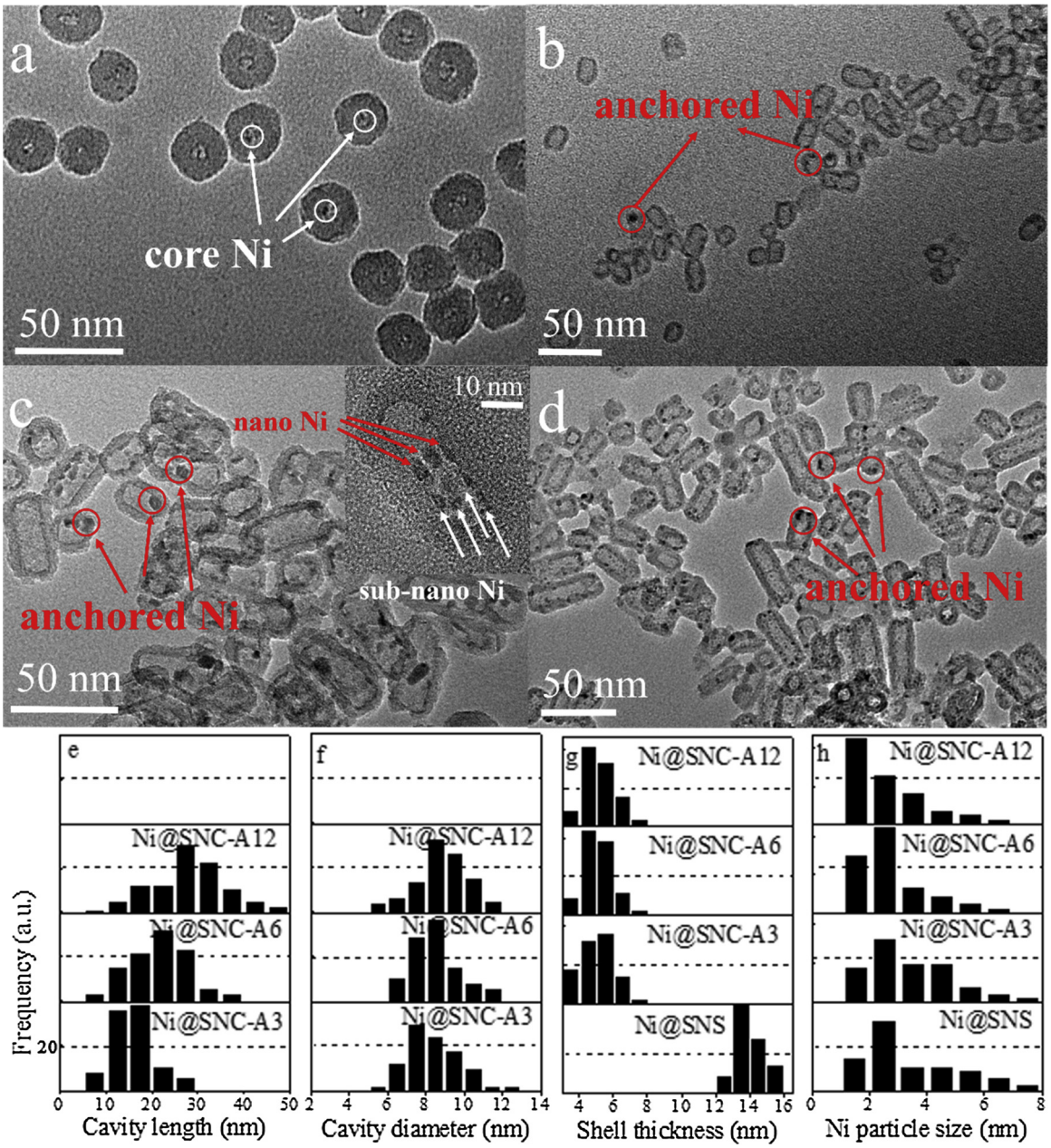

Fig. 1. Transmission electron microscope (TEM) images of (a) Ni@SNS, (b) Ni@SNC-A3, (c) Ni@SNC-A6, (d) Ni@SNC-A12 and parameter statistics of (e) cavity length, (f) cavity diameter, (g) shell thickness, (h) Ni particle size for the Ni@SiO_2 catalysts with different inner cavities determined from TEM images; the figure inset (c) shows the high resolution TEM image of a monomer capsule with distinct sub-nano and nano Ni particles.

the catalysts performance.

Our Ni@SNC catalysts exhibited a rarely-reported high carbon resistance with a high reactant conversion at a relatively low reaction temperature and ultra-high space velocity (700 °C and 60 L g^{-1} h^{-1}) (See the comparison of dry reforming catalysts concerning on the GHSV in Table S2 in ESI).

In comparison with the core-shell Ni@SNS catalyst which offers no inner space, the inner cavity space of Ni@SNC catalysts obviously improved the dispersion and accessibility of inner Ni sites, whilst also providing more active sites to the reactants [33,34]. Furthermore, the

Table 1
Physicochemical properties of the Ni@SiO_2 catalysts.

Catalysts	Ni loading[a] (wt%)	Surface area (m2 g^{-1})	Pore volume (cm3 g^{-1})	Average pore diameter (nm)	H2 desorption[b] (μmol g^{-1})	Ni dispersion[b] (%)
Ni@SNS	10.0	104	0.64	12.8	66	7.9
Ni@SNC-A3	12.2	265	0.78	9.3	95	10.3
Ni@SNC-A6	12.3	223	0.77	11.1	148	14.4
Ni@SNC-A12	12.4	224	0.87	12.5	135	13.1

[a] Ni loading was determined from ICP-AES analysis.
[b] Ni dispersion was calculated from the H_2 chemisorption results.

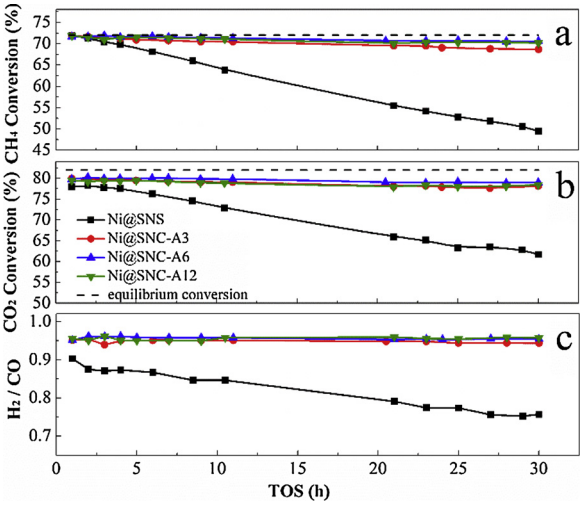

Fig. 2. Catalytic performance of the Ni@SiO_2 catalysts. (a) CH_4 conversion, (b) CO_2 conversion and (c) H_2/CO ratio. (1 atm, 700 °C, CH_4:CO_2 = 1:1, GHSV 60 L g^{-1} h^{-1}).

inner cavity space of an individual capsule can potentially function as an expansive "micro-reactor" independently, where the adsorption/transportation of reactants over Ni sites can be enhanced, facilitating a more efficient desorption of both reaction intermediates and products from the Ni sites under these high space velocity conditions [43]. It is our view that this prevents the accumulation of the inert carbon coking, as will be evidenced in our post-reaction studies.

3.3. Post-reaction analysis and carbon identification

The amount of carbon deposition contained in the spent Ni@SiO_2 samples was quantified by thermogravimetric analysis (TGA) (Fig. 3a). The excellent anti-coking ability of Ni@SNC capsule catalysts was clearly demonstrated by the negligible carbon deposition, as only 1.5 wt.% weight loss was observed over Ni@SNC-A6 catalyst while the carbon deposition on Ni@SNC-A3 and Ni@SNC-A12 catalysts were 3.0 wt.% and 2.5 wt.%, respectively. In contrast, the corresponding weight loss of carbon over Ni@SNS catalyst was as high as 37.5%. It is usually advanced that a confined core-shell structure is conducive to the inhibition of carbon deposition on catalyst surface [26,27]. We therefore highlight again that our catalytic tests were performed under a more stringent condition of a high GHSV of 60 L g^{-1} h^{-1} without dilution, which we attribute as the main reason for the high carbon deposition in Ni@SNS catalyst.

It is well established that for all the metal catalyzed (gas–solid) reactions we encounter, the overall process may be broken down into five constituent steps, viz: (i) transport of the reactants to the catalyst, (ii) adsorption of the reactants on the catalyst, (iii) interaction of adsorbed reactants, (iv) desorption of product from the catalyst, and (v) transport of product away from the catalyst. Steps (i) and (v) involve no chemical change, although in practice they can be rate-limiting and of obvious relevance to our systems involving a highly porous host for the catalyst (Fig. 1 and Table 1). Steps (ii) to (iv) do involve chemical changes and provided one of these is rate-limiting, the reaction will obey the Arrhenius equation. Thus the elementary steps of reactant transport/adsorption and carbon intermediate accumulation [44,45] (steps i to iii) could be significant and potentially detrimental to the entire process under these high space velocity conditions. As schematically revealed in Scheme 3a and frequently reported by other researchers [46–48], the unique capsule environment around the Ni cores can function as a micro-reactor in which the reactant molecules are enriched under the confined space offering a large volume. The consequence is enhanced transport/adsorption and catalytic reaction (C* + CO_2 = 2CO) on the metal surfaces (Scheme 3 a and b), which inhibit the coke accumulation over Ni@SNC.

In contrast, high carbon deposition on the spent Ni@SNS catalyst is considered to arise as a result of its limited inner space, causing a very low carbon elimination rate/ability which is much slower/weaker than that of the carbon formation (methane cracking) rate under a high methane feed rate. Moreover, since the limited inner cavity space of Ni@SNS favors Ni particle agglomeration during the reactions, the

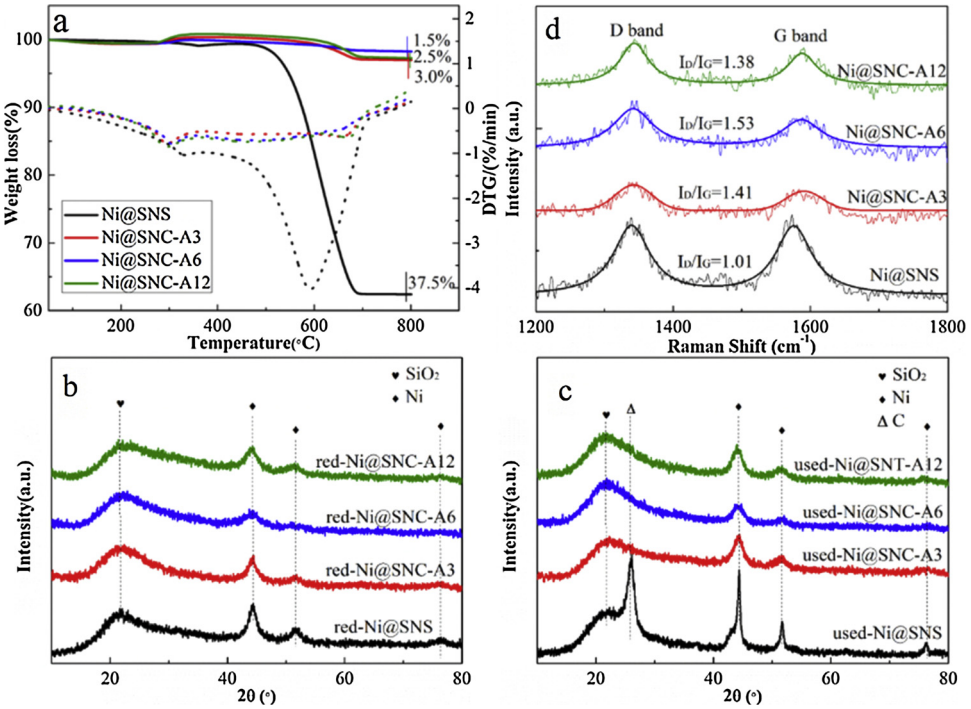

Fig. 3. (a) TGA-DTA patterns of spent Ni@SiO_2 catalysts; (b) and (c) are the XRD patterns of the reduced and spent Ni@SiO_2 catalysts; (d) Raman spectra of the spent Ni@SiO_2 catalysts after dry reforming of methane in high-space-velocity.

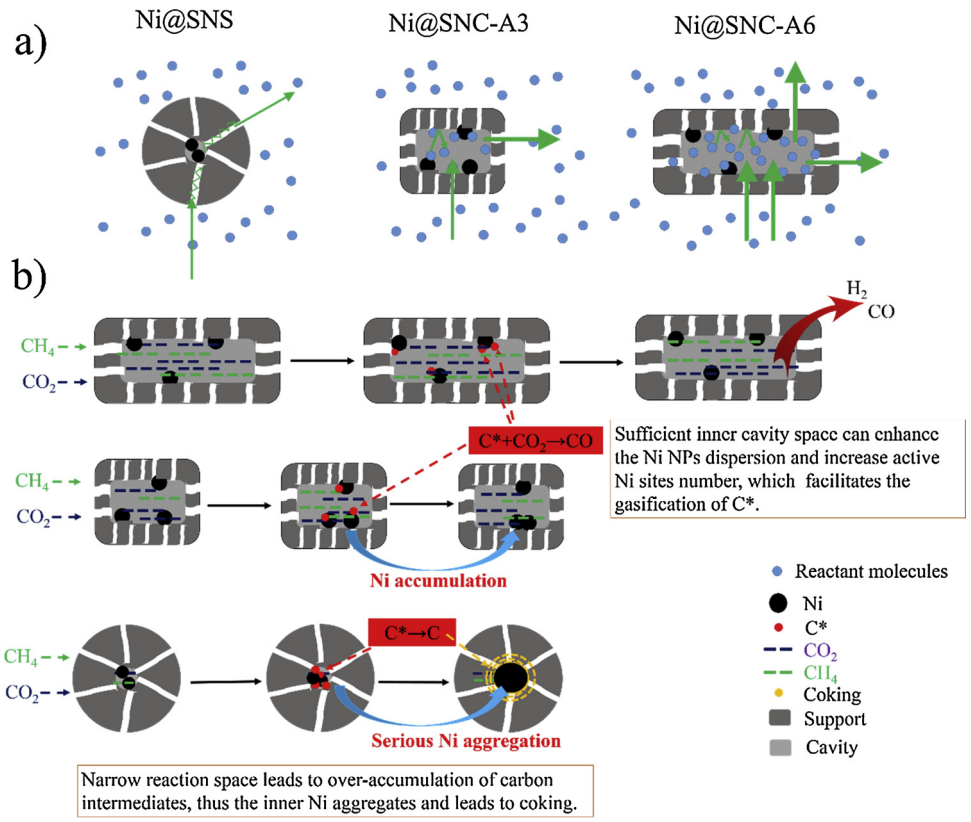

Scheme 3. (a) Schematic illustration of enhanced transport/adsorption and reaction in micro-reactors and (b) representation of Ni catalyst aggregation and carbon deposition mechanisms of the Ni@SiO_2 catalysts with various inner cavity dimensions in a typical DRM reaction process.

nascent, developing/larger Ni particles formed through any agglomeration process will otherwise accelerate large amounts of carbon deposition. On the contrary, due to the larger cavity space and greater availability, and variability of pores in the shell of Ni@SNC-A6,12, the catalysts allow for the fast conversion of the carbon intermediates and consequently the produced gaseous H_2/CO.

Differential thermal analysis (DTA) curves of Ni@SiO_2 catalysts shows mainly two endothermic peaks at around 300 °C and 670 °C. The peaks near 300 °C are attributed to the oxidation of metallic Ni [49] and amorphous carbon [50]. The peaks of spent Ni@SNC samples centred on 670 °C indicate the formation of tiny graphitic carbon as also reported elsewhere in the literature [10,51]. The broad peak observed at about 590 °C on spent Ni@SNS corresponds to the large amount of coating and/or filamentous carbons produced during the reactions, which has also been identified in TEM images.

In Fig. 4 we show TEM images of Ni@SNC-A3,6,12 capsule catalysts and Ni@SNS catalyst after DRM. As a general observation, no significant structural destruction occurred during the catalytic reactions; particularly, the important (host) yolk-shell framework of our Ni@SNC nanocapsule catalysts (Fig. 4a–d) remains intact. However, some Ni particles were found agglomerated in the Ni@SNC-A3 catalyst, while others remained unassociated. This is demonstrated by the statistical analysis of Ni particle distribution, where the number of sub-nanosized Ni particles in the used Ni@SNC-A3 catalyst is reduced, while the Ni particle size distributions of Ni@SNC-A6 and Ni@SNC-A12 catalysts have not changed significantly after the reaction was complete (Fig. 1h and Fig. 4f). Unlike the situation with Ni@SNC catalysts which presented excellent coking resistance, a large amount of graphitic carbon (filamentous and coating type) was produced and covered the aggregated Ni particles in spent Ni@SNS catalyst (Fig. S5). Importantly, some Ni particles were also significantly agglomerated and sintered into large particles with a particle size of > 12 nm. Our results in Fig. 4e and Figure S5b demonstrate clearly that graphitic (filamentous) carbon emanates out of the centre of a core-shell Ni@SNS with their “roots” in the aggregated Ni core. Since the processes of Ni aggregation and carbon formation are mutually reinforcing, once the Ni particles break through the constraint of the silica shell with the help of transport carbon along a graphene-Ni interface [52], they will become dissociated from of the accompanying “silica dress” and form larger Ni aggregates with characteristically larger Ni-Carbon core-shell structures, as shown in Fig. 4e. Similar Ni detachment and coke formation phenomena were also reported for other core-shell catalysts under rigid reaction conditions [53,54].

In Fig. 3b, c and Figure S3, we compare the X-ray diffraction (XRD) patterns of Ni@SiO_2 catalysts before and after the DRM. The reduced samples showed a strong broad diffraction peak at around 22.0° corresponding to the amorphous SiO_2 shell (JCPDS Card 29-0085), and the prominent diffraction peaks of metallic Ni at 44.4°, 51.6° and 76.5° (JCPDS card 01–1258). The corresponding Ni crystallite sizes were calculated using the Scherrer equation and are summarised in Table 2. Following the reduction process, Ni core particles grew slightly, and the larger particles were found in Ni@SNS catalyst which suggests that an appropriate larger inner cavity space is of vital importance in avoiding the sintering of metal catalyst particles under such a high temperature treatment.

Following the DRM processing, almost no changes were observed for the Ni@SNC samples, whereas the sharp XRD diffraction peaks of metallic Ni were detected on Ni@SNS catalysts, indicating significant Ni agglomeration and sintering during the reactions (Fig. 3c). The post-reaction Ni@SNS exhibited an obvious carbon diffraction peak at $2\theta = 26.2°$ (JCPDF 75–1621), whilst, importantly, no carbon signal was detected for any nanocapsule catalysts.

Although the Ni crystallite size of the used Ni@SNC-A3 catalyst was slightly increased, the Ni particles inside the inner cavities were still less than 6.5 nm; we attribute this to the special axial directional confinement of the capsule framework. This clearly indicates that the

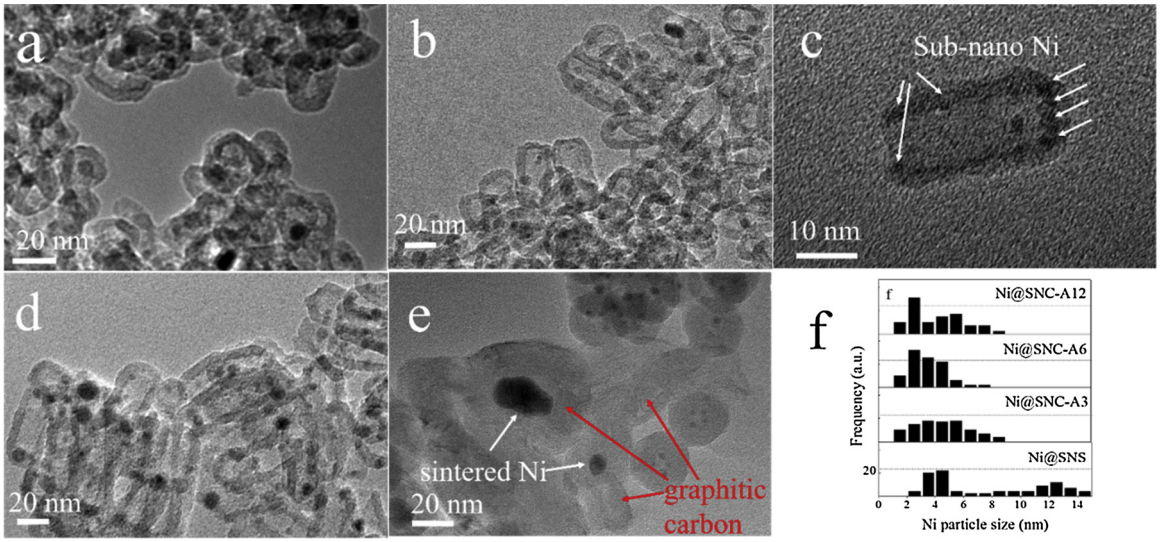

Fig. 4. TEM images of the used Ni@SiO_2 catalysts: (a) Ni@SNC-A3, (b) Ni@SNC-A6, (c) HR-TEM images of a nano monomer of the used Ni@SNC-A6 which showed no metal agglomeration and carbonaceous species existence, (d) Ni@SNC-A12, (e) Ni@SNS, and (f) Ni particle size statistics of the used Ni@SiO_2 catalysts.

Table 2
Nickel particle sizes of different Ni@SiO_2 catalysts before and after reactions.

Catalysts	TEM[a] (nm)		XRD[b] (nm)		
	d_{NiO}	$d_{Ni\text{-}used}$	d_{NiO}	d_{Ni}	$d_{Ni\text{-}used}$
Ni@SNS	2.8 ± 0.7	7.1 ± 3.6	3.9	5.5	12.1
Ni@SNC-A3	2.7 ± 1.4	4.4 ± 1.9	4.2	4.7	6.3
Ni@SNC-A6	2.2 ± 0.8	3.2 ± 1.3	2.0	2.1	3.2
Ni@SNC-A12	2.9 ± 1.3	3.9 ± 1.7	2.9	3.6	4.8

[a] The nickel particle sizes were determined from the average metal particle size in TEM images.
[b] The nickel crystalline size were determined via Scherrer's equation from the (200) plane of NiO and the (111) plane of Ni in XRD patterns.

active Ni nanoparticle catalyst can -importantly- be preserved in its low nuclearity state and thus suppresses any inert/graphitic carbon deposition; it is recognized that the critical minimum metal size requirement for the initiation of inert carbon formation is some 7 nm [55–57] (which could also be partially clarified by our Figure S5).

The Raman spectrum of the spent Ni@SNC and Ni@SNS catalysts is given in Fig. 3d. Two peaks at ca.1340 cm^{-1} and 1575 cm^{-1} were observed and in general they represent two types of carbon states, i.e. the former is attributed to the D-band peak showing the active amorphous carbon and the latter G-band peak representing the graphitic carbon species. The highest I_D/I_G (area intensity ratio of D band to G band) value of Ni@SNC-A6 sample is 1.53 while only 1.01 was obtained on the spent Ni@SNS catalyst. Moreover, it can be seen that Ni@SNC catalysts give much larger I_D/I_G values than Ni@SNS catalyst, indicating the largest carbon deposition on Ni@SNC-A3,6,12 catalysts consists of amorphous carbon [58], which is more easily eliminated/converted than the graphitic coating and filamentous carbon found in the Ni@SNS catalyst. Incorporating this with our TGA analysis in which a negligible amount of carbon was found in the Ni@SNC-A6 catalysts after DRM, it therefore suggests that an appropriate inner cavity size of Ni@SNC can prevent the growth of inert carbon in order to achieve maximum coking resistance.

3.4. Kinetic study on Ni@SNC nanocapsule catalysts in DRM to determine the effect of inner cavity space

In order to further investigate the effect of different inner cavities in Ni@SNC-A3,6,12 capsule catalysts, kinetic analysis was carried out

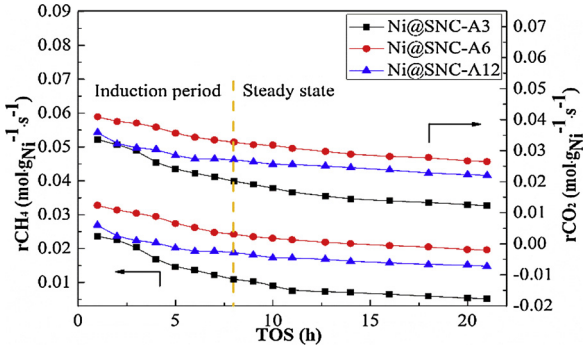

Fig. 5. Specific activities of the Ni@SNC catalysts in DRM under differential reaction condition. (1 atm, 700 °C, CH_4:CO_2 = 1:1, GHSV 1440 L g^{-1} h^{-1}).

under differential conditions [44,59] with extremely high GHSV value of 1440 L g_{cat}^{-1} h^{-1}. As a general observation, the Ni@SNC-A6 catalyst gave higher CH_4 and CO_2 reaction rates (namely r_{CH4} and r_{CO2}, in Fig. 5) than that of other Ni@SNC-A3 and Ni@SNC-A12 catalysts. Additionally, the induction period (namely the transient state) of Ni@SNC-A6 and Ni@SNC-A12 catalysts was about 8 h on stream while the Ni@SNC-A3 catalyst experienced a longer time of 10 h; after that all these catalysts can experience a quasi-steady state.

We believe that there are two main reasons for this large difference between the induction period and the steady state. First, one always requires a certain timescale to achieve an equilibrium state between the carbon formation rate and carbon diffusion/elimination rate over the Ni catalyst surface [60,61]. Second, some of the super active nano Ni clusters need to undergo a reshaping or restructuring process to lower their high surface active energy, thus resulting in the partial decrease of the initial TOF during any induction period [62]. Therefore, The TOFs of these three catalysts were determined by the CH_4 reaction rate at 10 h on steady state (Table 3). From these results, the Ni@SNC-A6 showed the highest TOF value of 9.6 s^{-1} while 4.8 s^{-1} and 7.4 s^{-1} were obtained for the Ni@SNC-A3 and Ni@SNC-A12 catalysts, respectively. This indicates that various amounts of Ni active sites are present among these capsule catalysts and the sample Ni@SNC-A6 has the highest intrinsic activity. Furthermore, the Ni@SNC-A6 catalyst also showed the least deactivation rate among others, with only 1.4% h^{-1} observed (Table 3).

In addition, the temperature sensitivity of kinetic reaction rates over Ni@SNC was also examined under a steady state as shown in Fig. S6.

Table 3
TOFs and apparent *Ea* values of the different Ni@SiO_2 catalysts under steady state.

Catalysts	TOF[a]$_{CH4}$ (s^{-1})	R_{CH4} deactivation (% h^{-1})[b]	*Ea*[c] (kJ mol^{-1})			
			CH_4	CO_2	H_2	CO
Ni@SNC-A3	4.8 (6.7)	3.9	57.1 ± 4.6	58.0 ± 0.8	87.2 ± 2.7	60.0 ± 3.4
Ni@SNC-A6	9.6 (13.1)	1.4	53.2 ± 4.3	50.6 ± 4.6	71.7 ± 5.2	47.7 ± 3.1
Ni@SNC-A12	7.4 (9.1)	1.7	55.1 ± 0.6	57.0 ± 4.2	80.1 ± 7.0	58.2 ± 5.0

[a] Turn over frequency (TOF) of Ni@SNC at 700 °C for GHSV of 1440 and 3600 L g^{-1} h^{-1} was calculated by mol s^{-1} of converted CH_4 divided by molar of activity Ni at 10 h on stream.
[b] R_{CH4} deactivation rate = (initial R_{CH4} – final R_{CH4})/steady state time on stream.
[c] Apparent *Ea* values were calculated by the slope of Ln (TOF) versus 1/T in Figure S6.

The resulting activation energies, *Ea*, of CH_4 for the Ni@SNC catalysts (Table 3) were lower than a reported impregnated Ni/SiO_2 catalyst (*Ea* = 62.3 kJ/mol) [63], which we attribute to the favourable effect of the embedded structure of Ni@SNC catalysts on the activation energy. Moreover, the *Ea* values of CH_4 and CO_2 for the Ni@SNC-A6 (53.2 kJ mol^{-1} and 50.6 kJ mol^{-1}) were lower than that of Ni@SNC-A3 and Ni@SNC-A12 catalysts, clearly demonstrating that Ni@SNC-A6 catalyst can effectively reduce the energy barrier required for CH_4 and CO_2 activation due to its superior cavity space feature, providing the most active Ni sites.

3.5. The importance of inner cavity structure both for high catalytic activity and coking resistance

It is clear that sub-nano Ni particles (< 2.5 nm) are necessary for the high catalytic activity in DRM, and the limited growth/agglomeration of (inner) Ni particles can therefore maintain the activity of the intrinsic Ni sites during the reactions at high temperature. Moreover, this could subsequently suppress the formation of coking carbon at very high space velocity conditions. Based upon the special (tubular) dimension of the inner cavity structure in Ni@ SNC-A3,6,12 nanocapsule catalysts, and their high dispersion; this resulted in a high catalytic activity and also -critically- high stability for DRM under very high space velocity conditions.

Depending on the different sizes of the inner space of Ni@SNC-A3,6,12 catalysts, the Ni@SNC-A3 catalyst (which has relatively smaller capsule space) produced larger Ni particle size and relatively low dispersion compared to Ni@SNC-A6, A12 catalysts (characterized by H_2 chemisorption in Table 1). Moreover, the temperature programmed reduction (TPR) of Ni@SNC-A3,6,12 catalysts shows a strong metal-support interaction with the anchored Ni in the capsule; by deconvolution of the TPR profiles (Figure S4 and Table S2), the proportion of reduction peak area at high-temperature increased when the inner cavity space was prolonged, which also implies more anchored Ni active sites are presented in the Ni@SNC-A6,12 catalysts. Therefore, with the same Ni loading, the Ni@SNC-A6, A12 catalysts, containing fine capsule structure with appropriate inner cavities, are able to well preserve the extremely small, highly active and - importantly - independent catalytic Ni core particles under the reforming reaction conditions.

We now turn to a consideration of the excellent coke resistance of the Ni@SNC catalysts. As we previously recognised, the same carbon intermediates throughout the methane cracking are shared by the reforming of methane itself and the side reactions of coking [52]. Accordingly, two strategies can be implemented to directly inhibit the deleterious coke formation during the DRM: The first is to inhibit the inert carbon nucleation/deposition (Route 1) and the second is to rapidly eliminate any developing carbon intermediates (Route 2). With the sealed two-dimensional-confined yolk-shell structure acting as a hard anti-coking framework, Ni@SNC catalysts can effectively inhibit the formation of morphological inert carbon such as filamentous and coating carbon as evidenced in our results. Importantly, it is known that the nucleation process or carbon deposition always involves the involvement of cooperating Ni clusters, a process prone to occur over large (high nuclearity) Ni particles above a critical minimum metal size of some 7 nm [64]. Accepting that, the sub-nano and nano Ni particles (< 5 nm) in the inner cavity are therefore well-protected by the special axial directional confinement of the encompassing capsule framework, and thus the Ni@SNC catalysts demonstrate an impressive anti-sintering ability even at the high temperatures of this process.

Furthermore, compared to the solid core-shell structure, a yolk-shell monomer which preserves a large inner cavity is highly beneficial for the gas transfer processes. Thus, rapid gasification of carbon intermediates can be achieved; consequently improving the catalytic activity which has also been frequently reported [25,53,65]. However, it must be pointed out that most of the spherical yolk-shell structures (with a diameter > 20 nm) have poor structural stability and their silica shells tend to crosslink and collapse with the presence of water (through RWGS) at high temperatures [66,67]. Such a process actively promotes the escape of Ni core particles, their aggregation as well as the evolving coke formation. In contrast, the synthesised Ni@SNC-A3, A6, A12 nanocapsule catalysts show exceptional stability against structural collapse during the DRM, which we believe arises from their robust and recalcitrant silica shell in a small radius dimension (i.d. < 6.5 nm); therefore the required hard anti-coking structure is protected and maintained.

Finally, it is important to note here that although there is no significant difference in terms of catalytic activity and coke resistance found over Ni@SNC catalysts whose inner cavity size is different, the extended inner cavity of the Ni@SiO_2 structure provides more independent sub-nano Ni particles having strongly anchored catalyst sites through highly effective geometric metal-support interactions, as schematized in Scheme 3 (and also reflected in the TEM, XRD, TPR and H_2 chemisorption properties). This strong geometric metal-support interaction will naturally reduce the mobility of the sub-nano Ni particles – even under high temperature conditions – and thus effectively suppress any aggregation of the catalytic Ni nanoparticles. As the sub-nano Ni particles will have larger active surface area and therefore provide more active centres, the increase of these active sites from Ni@SNS to Ni@SNC-A6 can drastically accelerate the gasification of activate carbon intermediates during the dry reforming reaction. Furthermore, we assume the increase of inner “micro-reactor” cavity space could also lift active site surface carbon (CO) desorption efficiency inside the capsule according to Le Chatelier’s principle [68], thus increasing the intrinsic catalytic activity and stability. However, despite these advantages of increased inner space, an *over-spacious* interior cavity can also be detrimental as the capsule framework will change from quasi-zero-dimensional to one-dimensional structure, partially losing the geometric confinement which prohibits on the reshaping/movement of Ni clusters and the diffusion of carbon species on the Ni surface [62]. Consequently, this could impair the necessary hard anti-coking capacity in the tubular direction, such as Ni@SNC-A12 sample compared to the Ni@SNC-A6 sample, where slightly more carbon accumulated together with larger Ni particles being produced.

4. Conclusion

A series of tubular yolk-shell Ni@SiO_2 nanocapsule (SNC) catalysts with tunable inner cavity dimensions and ultrafine Ni catalyst particles (< 5 nm) have been successfully prepared using a facile reverse micelle method. We hope to have highlighted the critical importance of inner cavity space within Ni@SNC catalysts for excellent coking resistance in the high-space-velocity dry reforming of methane.

The Ni@SNC catalysts were obtained with almost constant cavity diameter and shell thickness of around 9.0 nm and 5.0 nm, respectively. The different inner cavity lengths of catalysts were well-controlled by varying the aging time during the preparation; as a result, different Ni@SNC catalysts with average inner cavity lengths of 5–50 nm were successfully synthesized. Compared with a core-shell Ni@SNS sample, the necessity of larger inner cavity space is of vital importance in providing sufficient inner room for the surviving of small, independent and highly active Ni core particles, as well as the elimination of absorbed carbon intermediates over the active Ni site under very high space velocity conditions. Most importantly, the unique two dimensional confined structure with recalcitrant silica shell in a small radius dimension (i.d. < 6.5 nm) can therefore act as a hard anti-coking framework for the growth of inert carbon species such as carbon nanotubes/nanospheres etc. This important feature facilitates a high coking resistance for the process of high-space-velocity DRM. However, a cautionary point is that despite the advantages of inner space, an over-spacious interior cavity could reduce any anti-coking ability.

We believe that this work highlights the potential of these advances for an industrially relevant co-utilisation process involving both the greenhouse gases, CO_2 and CH_4, to produce synthesis gas as a feedstock to produce valuable products such as chemicals or fuels. DRM using these catalyst systems is one of the few options where one can envisage large scale chemical production with an environmentally relevant - that is, a large - amount of CO_2 utilisation.

Declaration of Competing Interest

The authors declare that they have no known competing financial interests or personal relationships that could have appeared to influence the work reported in this paper.

Acknowledgements

We are grateful for financial support from the National Natural Science Foundation of China (21603127), the Natural Science Foundation of Shanxi Province (201601D202020) and KACST, Saudi Arabia for their support of KOPRC. We also thank EPSRC (UK) and Shanxi University Future Development Foundation for the support of Dr Tiancun Xiao.

Appendix A. Supplementary data

Supplementary material related to this article can be found, in the online version, at doi:https://doi.org/10.1016/j.apcatb.2019.118019.

References

[1] F. Birol, World Energy Outlook 2018, France by DESK: International Energy Agency, (2018).
[2] J.L. Bubier, T.R. Moore, An ecological perspective on methane emissions from northern wetlands, Trends Ecol. Evol. (Amst.) 9 (1994) 460–464.
[3] H. Rodhe, A comparison of the contribution of various gases to the greenhouse-effect, Science 248 (1990) 1217–1219.
[4] H.R. Liu, S.Y. Xu, G.L. Zhou, G.C. Huang, S.Y. Huang, K. Xiong, CO2 hydrogenation to methane over Co/KIT-6 catalyst: effect of reduction temperature, Chem. Eng. J. 351 (2018) 65–73.
[5] X. Jiang, N. Koizumi, X.W. Guo, C.S. Song, Bimetallic Pd-Cu catalysts for selective CO2 hydrogenation to methanol, Appl. Catal. B: Environ. 170 (2015) 173–185.
[6] P. Moreno-Garcia, N. Schlegel, A. Zanetti, A.C. Lopez, M.D. Galvez-Vazquez, A. Dutta, M. Rahaman, P. Broekmann, Selective electrochemical reduction of CO2 to CO on zn-based foams produced by Cu2+ and template-assisted electrodeposition, ACS Appl. Mater. Interfaces 10 (2018) 31355–31365.
[7] S. Takenaka, H. Umebayashi, E. Tanabe, H. Matsune, M. Kishida, Specific performance of silica-coated Ni catalysts for the partial oxidation of methane to synthesis gas, J. Catal. 245 (2007) 392–400.
[8] D. Laprune, C. Theodoridi, A. Tuel, D. Farrusseng, F.C. Meunier, Effect of poly-aromatic tars on the activity for methane steam reforming of nickel particles embedded in silicalite-1, Appl. Catal. B: Environ. 204 (2017) 515–524.
[9] P. Xu, Z.M. Zhou, C.J. Zhao, Z.M. Cheng, Catalytic performance of Ni/CaO-Ca5Al6O14 bifunctional catalyst extrudate in sorption-enhanced steam methane reforming, Catal. Today 259 (2016) 347–353.
[10] Q. Zhang, T. Zhang, Y. Shi, B. Zhao, M. Wang, Q. Liu, J. Wang, K. Long, Y. Duan, P. Ning, A sintering and carbon-resistant Ni-SBA-15 catalyst prepared by solid-state grinding method for dry reforming of methane, J. CO2 Util. 17 (2017) 10–19.
[11] W. Nimwattanakul, A. Luengnaruemitchai, S. Jitkarnka, Potential of Ni supported on clinoptilolite catalysts for carbon dioxide reforming of methane, Int. J. Hydrogen Energy 31 (2006) 93–100.
[12] A.G. Bhavani, W.Y. Kim, J.S. Lee, Barium substituted lanthanum manganite perovskite for CO2 reforming of methane, ACS Catal. 3 (2013) 1537–1544.
[13] G. Centi, E.A. Quadrelli, S. Perathoner, Catalysis for CO2 conversion: a key technology for rapid introduction of renewable energy in the value chain of chemical industries, Energy Environ. Sci. 6 (2013) 1711–1731.
[14] C.-j. Liu, J. Ye, J. Jiang, Y. Pan, Progresses in the preparation of coke resistant ni-based catalyst for steam and CO2 reforming of methane, Chemcatchem 3 (2011) 529–541.
[15] G. Zhang, J. Liu, Y. Xu, Y. Sun, Ordered mesoporous Ni/Silica-carbon as an efficient and stable catalyst for CO2 reforming of methane, Int. J. Hydrogen Energy 44 (2019) 4809–4820.
[16] M.M. Nair, S. Kaliaguine, F. Kleitz, Nanocast LaNiO3 Perovskites as Precursors for the preparation of coke-resistant dry reforming catalysts, ACS Catal. 4 (2014) 3837–3846.
[17] Y. Cao, M. Lu, J. Fang, L. Shi, D. Zhang, Hexagonal boron nitride supported mesoSiO2-confined Ni catalysts for dry reforming of methane, Chem. Commun. (Camb.) 53 (2017) 7549–7552.
[18] Y. Cao, P. Maitarad, M. Gao, T. Taketsugu, H. Li, T. Yan, L. Shi, D. Zhang, Defect-induced efficient dry reforming of methane over two-dimensional Ni/h-boron nitride nanosheet catalysts, Appl. Catal. B 238 (2018) 51–60.
[19] K. Bu, S. Kuboon, J. Deng, H. Li, T. Yan, G. Chen, L. Shi, D. Zhang, Methane dry reforming over boron nitride interface-confined and LDHs-derived Ni catalysts, Appl. Catal. B 252 (2019) 86–97.
[20] A. Vita, G. Cristiano, C. Italiano, L. Pino, S. Specchia, Syngas production by methane Oxy-steam reforming on Me/CeO2 (me = Rh, Pt, Ni) catalyst lined on cordierite monoliths, Appl. Catal. B: Environ. 162 (2015) 551–563.
[21] J.L. Lu, B.S. Fu, M.C. Kung, G.M. Xiao, J.W. Elam, H.H. Kung, P.C. Stair, Coking- and sintering-resistant palladium catalysts achieved through atomic layer deposition, Science 335 (2012) 1205–1208.
[22] H. Ma, L. Zeng, H. Tian, D. Li, X. Wang, X. Li, J. Gong, Efficient hydrogen production from ethanol steam reforming over La-modified ordered mesoporous Ni-based catalysts, Appl. Catal. B: Environ. 181 (2016) 321–331.
[23] N.N. Sun, X. Wen, F. Wang, W. Wei, Y.H. Sun, Effect of pore structure on Ni catalyst for CO2 reforming of CH4, Energy Environ. Sci. 3 (2010) 366–369.
[24] Z.-Y. Lim, C. Wu, W.G. Wang, K.-L. Choy, H. Yin, Porosity effect on ZrO2 hollow shells and hydrothermal stability for catalytic steam reforming of methane, J. Mater. Chem. A Mater. Energy Sustain. 4 (2016) 153–159.
[25] J.C. Park, J.U. Bang, J. Lee, C.H. Ko, H. Song, Ni@SiO2 yolk-shell nanoreactor catalysts: high temperature stability and recyclability, J. Mater. Chem. 20 (2010) 1239–1246.
[26] F. Wang, L. Xu, W. Shi, Syngas production from CO2 reforming with methane over core-shell Ni@SiO2 catalysts, J. CO2 Util. 16 (2016) 318–327.
[27] J.S. Zhang, F.X. Li, Coke-resistant Ni@SiO2 catalyst for dry reforming of methane, Appl. Catal. B: Environ. 176 (2015) 513–521.
[28] K.A. Dahlberg, J.W. Schwank, Synthesis of Ni@SiO2 nanotube particles in a water-in-oil microemulsion template, Chem. Mater. 24 (2012) 2635–2644.
[29] Z. Li, L. Mo, Y. Kathiraser, S. Kawi, Yolk–satellite–shell structured Ni–yolk@ Ni@SiO2 nanocomposite: superb catalyst toward methane CO2 reforming reaction, ACS Catal. 4 (2014) 1526–1536.
[30] C. Wang, Y. Qiu, X. Zhang, Y. Zhang, N. Sun, Y. Zhao, Geometric design of a Ni@silica nano-capsule catalyst with superb methane dry reforming stability: enhanced confinement effect over the nickel site anchoring inside a capsule shell with an appropriate inner cavity, Catal. Sci. Technol. 8 (2018) 4877–4890.
[31] C.X. Zhang, W.C. Zhu, S.R. Li, G.W. Wu, X.B. Ma, X. Wang, J.L. Gong, Sintering-resistant Ni-based reforming catalysts obtained via the nanoconfinement effect, Chem. Commun. (Camb.) 49 (2013) 9383–9385.
[32] Z. Bian, I.Y. Suryawinata, S. Kawi, Highly carbon resistant multicore-shell catalyst derived from Ni-Mg phyllosilicate nanotubes@silica for dry reforming of methane, Appl. Catal. B 195 (2016) 1–8.
[33] L. Wang, D. Li, M. Koike, H. Watanabe, Y. Xu, Y. Nakagawa, K. Tomishige, Catalytic performance and characterization of Ni-Co catalysts for the steam reforming of biomass tar to synthesis gas, Fuel 112 (2013) 654–661.
[34] X.Y. Zhao, H.R. Li, J.P. Zhang, L.Y. Shi, D.S. Zhang, Design and synthesis of NiCe@m-SiO2 yolk-shell framework catalysts with improved coke- and sintering-resistance in dry reforming of methane, Int. J. Hydrogen Energy 41 (2016) 2447–2456.
[35] K.A. Dahlberg, J.W. Schwank, Synthesis of Ni@ SiO2 nanotube particles in a water-in-oil microemulsion template, Chem. Mater. 24 (2012) 2635–2644.

[36] C. Gao, Z. Lu, Y. Yin, Gram-scale synthesis of silica nanotubes with controlled aspect ratios by templating of nickel-hydrazine complex nanorods, Langmuir 27 (2011) 12201–12208.
[37] M.J. Joralemon, S. McRae, T. Emrick, PEGylated polymers for medicine: from conjugation to self-assembled systems, Chem. Commun. (Camb.) 46 (2010) 1377–1393.
[38] P. Khullar, A. Mahal, V. Singh, T.S. Banipal, G. Kaur, M.S. Bakshi, How PEO-PPO-PEO triblock polymer micelles control the synthesis of gold nanoparticles: temperature and hydrophobic effects, Langmuir 26 (2010) 11363–11371.
[39] Z. Li, C. Han, J. Shen, Reduction of Ni2+ hydrazine in solution for the preparation of nickel nano-particles, J. Mater. Sci. 41 (2006) 3473–3480.
[40] J. Zhang, Z. Ge, X. Jiang, P.A. Hassan, S. Liu, Stopped-flow kinetic studies of sphere-to-rod transitions of sodium alkyl sulfate micelles induced by hydrotropic salt, J. Colloid Interf. Sci. 316 (2007) 796–802.
[41] M. Tornblom, U. Henriksson, Effect of solubilization of aliphatic hydrocarbons on size and shape of rodlike C(16)TABr micelles studied by H-2 NMR relaxation, J. Phys. Chem. B 101 (1997) 6028–6035.
[42] Z. Bao, Y. Lu, J. Han, Y. Li, F. Yu, Highly active and stable Ni–based bimodal pore catalyst for dry reforming of methane, Appl. Catal. A Gen. 491 (2015) 116–126.
[43] L.H. Yao, Y.X. Li, J. Zhao, W.J. Ji, C.T. Au, Core-shell structured nanoparticles (M@SiO(2), Al(2)O(3), MgO; M = Fe, Co, Ni, Ru) and their application in CO(x)-free H(2) production via NH(3) decomposition, Catal. Today 158 (2010) 401–408.
[44] J.F. Munera, S. Irusta, L.M. Cornaglia, E.A. Lombardo, D.V. Cesar, M. Schmal, Kinetics and reaction pathway of the CO2 reforming of methane on Rh supported on lanthanum-based solid, J. Catal. 245 (2007) 25–34.
[45] C. Wang, N. Sun, M. Kang, X. Wen, N. Zhao, F. Xiao, W. Wei, T. Zhao, Y. Sun, The bi-functional mechanism of CH4 dry reforming over a Ni-CaO-ZrO2 catalyst: further evidence via the identification of the active sites and kinetic studies, Catal. Sci. Technol. 3 (2013) 2435–2443.
[46] S.H. Joo, J.Y. Park, C.-K. Tsung, Y. Yamada, P. Yang, G.A. Somorjai, Thermally stable Pt/mesoporous silica core–shell nanocatalysts for high-temperature reactions, Nat. Mater. 8 (2008) 126.
[47] X. Pan, X. Bao, Reactions over catalysts confined in carbon nanotubes, Chem. Commun. (Camb.) (2008) 6271–6281.
[48] Y. Li, L. Yao, Y. Song, S. Liu, J. Zhao, W. Ji, C.-T. Au, Core-shell structured microcapsular-like Ru@SiO2 reactor for efficient generation of COx-free hydrogen through ammonia decomposition, Chem. Commun. (Camb.) 46 (2010) 5298–5300.
[49] N. Wang, X. Yu, K. Shen, W. Chu, W. Qian, Synthesis, characterization and catalytic performance of MgO-coated Ni/SBA-15 catalysts for methane dry reforming to syngas and hydrogen, Int. J. Hydrogen Energy 38 (2013) 9718–9731.
[50] D. Liu, Y. Wang, D. Shi, X. Jia, X. Wang, A. Borgna, R. Lau, Y. Yang, Methane reforming with carbon dioxide over a Ni/ZiO(2)-SiO2 catalyst: influence of pre-treatment gas atmospheres, Int. J. Hydrogen Energy 37 (2012) 10135–10144.
[51] E.C. Lovell, A. Fuller, J. Scott, R. Amal, Enhancing Ni-SiO2 catalysts for the carbon dioxide reforming of methane: reduction-oxidation-reduction pre-treatment, Appl. Catal. B: Environ. 199 (2016) 155–165.
[52] S. Helveg, C. Lopez-Cartes, J. Sehested, P.L. Hansen, B.S. Clausen, J.R. Rostrup-Nielsen, F. Abild-Pedersen, J.K. Norskov, Atomic-scale imaging of carbon nanofibre growth, Nature 427 (2004) 426–429.
[53] W. Yang, H. Liu, Y. Li, J. Zhang, H. Wu, D. He, Properties of yolk–shell structured Ni@SiO2 nanocatalyst and its catalytic performance in carbon dioxide reforming of methane to syngas, Catal. Today 259 (2016) 438–445.
[54] Y. Zhao, H. Li, H. Li, NiCo@SiO2 core-shell catalyst with high activity and long lifetime for CO2 conversion through DRM reaction, Nano Energy 45 (2018) 101–108.
[55] J.H. Kim, D.J. Suh, T.J. Park, K.L. Kim, Effect of metal particle size on coking during CO2 reforming of CH4 over Ni-alumina aerogel catalysts, Appl. Catal. A Gen. 197 (2000) 191–200.
[56] S. Tang, L. Ji, J. Lin, H.C. Zeng, K.L. Tan, K. Li, CO2 reforming of methane to synthesis gas over sol-gel-made Ni/gamma-Al2O3 catalysts from organometallic precursors, J. Catal. 194 (2000) 424–430.
[57] L. Chen, Q.S. Zhu, R.F. Wu, Effect of Co-Ni ratio on the activity and stability of Co-Ni bimetallic aerogel catalyst for methane Oxy-CO2 reforming, Int. J. Hydrogen Energy 36 (2011) 2128–2136.
[58] Z.X. Yang, Y.D. Xia, R. Mokaya, Enhanced hydrogen storage capacity of high surface area zeolite-like carbon materials, J. Am. Chem. Soc. 129 (2007) 1673–1679.
[59] X.E. Verykios, Catalytic dry reforming of natural gas for the production of chemicals and hydrogen, Int. J. Hydrogen Energy 28 (2003) 1045–1063.
[60] V.A. Tsipouriari, X.E. Verykios, Kinetic study of the catalytic reforming of methane with carbon dioxide to synthesis gas over Ni/La2O3 catalyst, Catal. Today 64 (2001) 83–90.
[61] C. Wang, N. Sun, N. Zhao, W. Wei, J. Zhang, T. Zhao, Y. Sun, C. Sun, H. Liu, C.E. Snape, The properties of individual carbon residuals and their influence on the deactivation of Ni–CaO–ZrO2 catalysts in CH4 dry reforming, ChemCatChem 6 (2014) 640–648.
[62] Z. Li, Z. Wang, S. Kawi, Sintering and coke resistant core/yolk shell catalyst for hydrocarbon reforming, ChemCatChem 11 (2019) 202–224.
[63] J.M. Wei, E. Iglesia, Isotopic and kinetic assessment of the mechanism of reactions of CH4 with CO2 or H2O to form synthesis gas and carbon on nickel catalysts, J. Catal. 224 (2004) 370–383.
[64] R. Pereniguez, V.M. Gonzalez-delaCruz, A. Caballero, J.P. Holgado, LaNiO3 as a precursor of Ni/La2O3 for CO2 reforming of CH4: effect of the presence of an amorphous NiO phase, Appl. Catal. B: Environ. 123 (2012) 324–332.
[65] Z. Li, L. Mo, Y. Kathiraser, S. Kawi, Yolk–satellite–shell structured Ni–Yolk@Ni@SiO2Nanocomposite: superb catalyst toward methane CO2 reforming reaction, ACS Catal. 4 (2014) 1526–1536.
[66] Z.W. Li, Y. Kathiraser, J. Ashok, U. Oemar, S. Kawi, Simultaneous tuning porosity and basicity of Nickel@Nickel-Magnesium phyllosilicate core-shell catalysts for CO2 reforming of CH4, Langmuir 30 (2014) 14694–14705.
[67] L.H. Yao, Y.X. Li, J. Zhao, W.J. Ji, C.T. Au, Core–shell structured nanoparticles (M@SiO2, Al2O3, MgO; M = Fe, Co, Ni, Ru) and their application in COx-free H2 production via NH3 decomposition, Catal. Today 158 (2010) 401–408.
[68] L.C. Buelens, V.V. Galvita, H. Poelman, C. Detavernier, G.B. Marin, Super-dry reforming of methane intensifies CO2 utilization via Le Chatelier's principle, Science 354 (2016) 449–452.